Multiple-Wavelength Sensing of Jupiter During the Juno Mission's First Perijove Passage

G. S. Orton[1], T. Momary[1], A. P. Ingersoll[2], A. Adriani[3], C. J. Hansen[4], M. Janssen[1], J. Arballo[1], S. K. Atreya[4], S. Brown[1], M. Caplinger[5], D. Grassi[3], C. Li[1], M. L. Moriconi[3,6], A. Mura[3], G. Sindoni[3]

[1]Jet Propulsion Laboratory, California Institute of Technology, Pasadena, California, USA

[2]Division of Geological and Planetary Sciences, California Institute of Technology, Pasadena, California, USA

[3]INAF-Istituto di Astrofisica e Planetologia Spaziali, Roma, Italy

[4]University of Michigan, Ann Arbor, Michigan, USA

[5]Malin Space Science Systems, San Diego, California, USA

[6]CNR-Istituto di Scienze dell'Atmosfera e del Clima, Roma, Italy

Corresponding author: Glenn Orton (glenn.orton@jpl.nasa.gov)

Key Points:

- A high correlation between visibly dark clouds and 5-μm radiation extends only partially to microwave radiation.
- Spectroscopy at 5 μm and microwave radiometry agree on the abundance of ammonia near 5 bars, a value within the uncertainty of a determined by Galileo.
- Meridional dependence of deep atmospheric opacity is mostly consistent with other indirect tracers of vertical motions in the troposphere.

Abstract

We compare observations of Jupiter made around 2016 August 27 by Juno's JunoCam, JIRAM and MWR instruments near its closest approach to Jupiter, together with observations from NASA's Infrared Telescope Facility. There is a high correlation of the location of dark regions in JunoCam's visible images and JIRAM's maps at 5 μm, which is sensitive to variations of particulate opacity and gaseous NH_3 absorption near depths corresponding to atmospheric pressures of 6 bars or less. There are some substantial correlations between variations of 5-μm and microwave radiances that arise from similar dependence on variability of the opacity of gaseous NH_3 absorption. There are also significant exceptions that are likely due to the additional opacity of particulate scattering and absorption at 5 μm, demonstrating that high abundances of saturated gas and high particulate opacities are not uniformly correlated. JIRAM spectroscopy and the MWR derive consistent 5-bar NH_3 abundances, but they are lower than nominal Galileo results for the probe entry site. The high NH_3 abundance over a broad vertical range near the equator is consistent with vigorous vertical transport and with the distribution of some disequilibrium species used as indirect indicators of vertical motions. A possible slower rise of NH_3 abundance toward the poles, indicating a gradually increasing strength of upwelling circulation with latitude, is consistent with a rise of the abundances of tropospheric disequilibrium constituents, except the 330-mbar para-H_2 fraction. Its rise with latitude indicates the increasing strength of downwelling in the upper troposphere and lower stratosphere.

1 Introduction

Remote-sensing observations of Jupiter were made throughout the first close approach to Jupiter when scientific instruments were turned on, an epoch known as "perijove 1" (or PJ1) on August 27, 2016. Here we compare measurements of Jupiter that were taken at visible and near-infrared wavelengths contemporaneously with measurements of microwave thermal emission from the planet's deep atmosphere with minimal interference from the synchrotron radiation generated by Jupiter's magnetosphere. The latter is responsible for the obscuration of thermal radiation from the deep neutral atmosphere that plagues Earth-based observations in the microwave. We establish general relationships between visible cloud colors and cloud depths inferred from thermal emission in the near infrared. Moreover, we will also make the first comparison of characteristics of the deep troposphere with properties of the "weather layer" that can be detected relatively routinely from the visible and infrared, which will establish any coupling that may exist between different levels of the atmosphere. We will also compare properties of the deep atmosphere with properties that have been used indirectly to infer vertical motions of the atmosphere.

2 Materials and Methods

We present observations of Jupiter made by three of Juno's remote-sensing instruments: JunoCam, the education/public-outreach camera, the Jovian Infrared Auroral Mapper (JIRAM), and the MicroWave Radiometer (MWR). We select observations that overlap in spatial coverage of the planet, focusing specifically on measurements overlapping the limited spatial coverage of the MWR, 60º-130ºW and within 70ºS to 70ºN (Figure 1).

We also present contemporaneous ground-based near-infrared images from NASA's Infrared Telescope Facility (IRTF), and a contemporaneous image obtained in the red part of the visible spectrum from a small telescope near the time Juno's perijove passage for comparison with the spacecraft results. The IRTF near-infrared image used to provide a verification of the forward extrapolation of the more distant JIRAM observations that preceded the time of PJ1 passage by several hours. The small-telescope image is used to verify the geometric calibration and similar forward extrapolation of the JunoCam images, many of which were taken many hours before and after the time of PJ1 passage.

We make a direct visual comparison between the visible, near-infrared and microwave observations to verify that relationships between visible cloud color and cloud depth that were established by previous spacecraft at Jupiter and Earth-based measurements remain valid. We compare retrievals of gaseous NH_3 abundances from the JIRAM and MWR observations in the upper troposphere, and we compare MWR measurements of opacity much deeper in the atmosphere and their implications for vertical transport with other putative indirect measures of vertical motion from previous spacecraft and Earth-based measurements. Figure 1 provides an overview of the measurements we address.

3 Detailed Description of the Data

JunoCam. Color images in the visible spectrum are composited from images of Jupiter taken through red, green and blue ("RGB") filters by the education and public-outreach camera, JunoCam [Hansen et al. 2014]. Panel A of Figure 1 shows a mosaic of map-projected JunoCam images. We abbreviate image file names as follows: JNCE_2016240_00C06151_V01 is identified simply as file 6151. These files include not only "close-up" images taken within 2 hours of perijove passage, but those taken as a part of animation sequences during the inbound and outbound legs. The primary files used to compare with the regions of the atmosphere covered by JIRAM and the MWR include files 6151, 6159, 6160, and 6180, with some inputs from files 6171, 6174 and 6186. The spatial resolution on Jupiter ranged from tens to hundreds of kilometers.

JIRAM. JIRAM [Adriani et al. 2014] made a series of maps of radiance from Jupiter. One portion of these maps were made using the 5μm-filtered camera in a series of imaging sequences. The highest-resolution maps have been combined in a mosaic to cover the track of MWR observations and the ones closest to the planet were obtained about 5 hours before the perijove with a mean spatial resolution of 110 km. The 5-μm map is shown in Panel B of Figure 1. The other maps of the mosaic were obtained at greater distances from Jupiter and together comprised a global map. Geometric information for the Jupiter maps have been computed through the support of the SPICE standard system [Acton 1996] by using the spacecraft's trajectory and attitude kernels and JIRAM scanning mirror telemetry, and used to geo-reference each required planetary region. With reference to the Jupiter datum and ellipsoid, included in the ENVI-IDL utilities, planetocentric System-III coordinates have been used to geo-locate the JIRAM data and a Mercator projection, implemented with accurate equatorial and polar radii and suitable false easting and northing, has been applied to map the region where MWR and JIRAM acquisitions overlap. The JIRAM spatial resolutions of the maps used in Figure 1 differ with the latitude as 5μm images were acquired at different distances during the inbound (equatorial and northern hemisphere) and in the outbound (southern hemisphere). The spatial resolutions in Figure 1 have been reported in

the Table 1. We also address second-order JIRAM products: retrievals of the ammonia (NH_3) volume mixing ratio (VMR) with a relative accuracy of 20% obtained from JIRAM 4.5-5 μm spectroscopy acquired between August 25 and 28.

Table 1. JIRAM spatial resolution

Latitudes	Spatial Resolution
65°S/50°S	380 km
50°S/20°S	250 km
20°S/20°N	110 km
20°S/50°N	250 km
50°N/65°N	380 km

MWR. The six independent microwave radiometers on Juno's MicroWave Radiometer experiment [Janssen et al. 2017a] scanned along a track close to the sub-spacecraft longitude at the time of perijove passage, as shown in Panel C of Figure 1, obtaining observations at each latitude from multiple emission angles. For this orbit, at each latitude longitudes of sequential observations shifted as a function of time as a result of Jupiter's rotation. In this article, we examine data taken by the MWR and consider nadir-based or nadir-equivalent observations only, such as those used in the derivation of the meridional variability of NH_3 with depth by Li et al. [2017]. A MWR map at 1.38 cm is shown in Panel D of Figure 1. Jupiter's rotation enabled the limited longitudinal sampling, and radiances were converted to their nadir equivalents using a quadratic fit to all data with emission angles between 0° and 50° and cubic interpolation across sampling gaps within the swath using a 2° grid spacing. Panels E, F and G represent nadir-equivalent longitudinally averaged results for 1.38 cm, 3.0 cm and 5.75 cm, respectively. These panels used a subset of brightness temperature data with emission angles within 5° of nadir, and taking the mean of 1° latitude bins. We also examine the retrieved NH_3 VMR from MWR observations itself.

We took advantage of the fact that NH_3 is by far the dominant microwave absorber in Jupiter's atmosphere to interpret the microwave spectrum measured at each point in latitude as due to a vertical distribution of NH_3 concentration [Li et al. 2017]. The retrieval of an ammonia concentration varying with latitude and atmospheric depth was accordingly obtained as described in Li et al [2017]. The uncertainty in the NH_3 absorption coefficient plus reasonable uncertainties involving model assumptions for atmospheric composition and temperature lapse rate combine to give a net uncertainty of about 20% in the concentration. The NH_3 VMR was found to vary more than 50% in both depth and latitude, from an asymptotic maximum of 360 ppmv at pressure levels below 50 – 100 bar to values varying from 120 ppmv to 320 ppmv around the 5-bar level.

Ground-based imaging. We also present a ground-based 5.1-μm image from NASA's Infrared Telescope Facility (IRTF) taken with the scientific-grade guide camera attached to the near-infrared moderate-resolution spectrometer SpeX [Rayner et al. 2003]. With Jupiter only 23° from the sun, the telescope dome and shutter needed to shade the IRTF's 3-meter primary mirror from direct sunlight. As a result, the primary mirror partially obscured and the background sky

level correspondingly increased compared with much less emissive sky. Absolute calibration was not possible, both because of this obscuration and the partly cloudy state of the sky over Mauna Kea during these observations. Panel C of Figure 1 shows a excerpt from a cylindrical projection of the IRTF image. Atmospheric seeing and diffraction limited the spatial resolution to the equivalent of ~1° in latitude or longitude at the equator.

4 Results

Figure 1 presents an overview of observations of Jupiter from all the data sources close to Juno's perijove-1 passage. A general comparison with the 5-μm JIRAM map reinforces a strong correlation between regions that are dark in the visible and bright at 5 μm**.** Conversely, regions that are visibly bright correspond to regions that are faint at 5 μm. This correlation has been made in a rigorous approach using high-spatial-resolution Galileo observations by the Near Infrared Mapping Spectrometer (NIMS) instrument, where a high correlation is found between bright 5-μm radiance and low long-wavelength visible and near-infrared reflectivity at "continuum" wavelengths away from strong gaseous absorption features [Irwin et al. 2001]. In this encounter by Juno, prominent dark regions around light- colored ovals correspond to particularly bright peripheries of these features at 5 μm. The most prominent of these are the ovals at 38°S, but the correspondence extends down to extremely small spatial scales, such as the ovals with dark peripheries poleward of 40° latitude in either hemisphere. These have been noted in earlier Earth-based observations [de Pater et al. 2010, 2011] and the ovals with the highest contrast are a particular focus of JIRAM study described in this issue [Sindoni et al. 2017]. We note also that the dark blue-gray discrete features near 7°N correspond to particularly bright features at 5 μm. These are known as 5-μm "hot spots", reported first by Terrile and Westphal [1977], and another focus of JIRAM study [Grassi et al. 2017]. These correspond to the blue-gray regions at this latitude in Panel A, a correlation that has been well established for these region [Owen and Terrile, 1981]. These regions have been characterized as the driest and most cloud-free regions in Jupiter [e.g. Terrile and Westphal 1977, Ortiz et al. 1998, Fletcher et al. 2016], and they are of specific interest because the Galileo probe descended into one of them [Orton et al. 1996, 1998]. A correlation between Juno measurements of the physical properties of the atmosphere in 5-μm hot spots and the Galileo probe results is considered an important element of closure in the study of Jupiter's atmosphere, providing a link between independent spacecraft results.

The opacity in the 5-μm window is controlled by the opacity of cloud particles, together with moderate gaseous NH_3 and weaker PH_3 and faint H_2O absorption [Grassi et al. 2010]. In absence of substantial cloud coverage in the upper troposphere (as found, for example, in 5-μm hot spots), radiation from this window can be sensitive as deep as the 6-bar atmospheric pressure level, although the average radiation emerges from the 4-5 bar level. It is useful to compare results from the JIRAM 5-μm maps and the MWR channels 4-6 which are sensitive to gaseous NH_3 absorption in the upper troposphere between the ~0.7- to 5-bar atmospheric pressure levels [Janssen et al. 2017b]. Such a comparison should enable a differentiation between gaseous and particulate opacity, given that the particles have been characterized as sub-micron in size (see, for example, Irwin et al. [2001]). A visual comparison between 5-μm radiances and MWR radiances can be made by comparing the 5-μm radiances in Panels B and C of Figure 1 with the limited-area map of MWR radiances in channel 6 (Panel D) and a representation of the nadir- equivalent MWR

radiances in its channels 6, 5, and 4 - in Panels E, F and G, respectively. A more quantitative comparison is provided by Figure 2, which compares the MWR brightness temperatures with the brightness temperatures equivalent to convolving radiances in the JIRAM high-resolution map with the MWR channel-6 angular sensitivity function.

There is a correlation of bright areas in both spectral regions in the North Equatorial Belt (NEB), which is generally bright at 5 μm between 7° and 14°N and in the MWR channels between 7° and 15°N-19°N (depending on the MWR channel), indicating both low cloud opacity and low NH_3 gaseous absorption relative to the rest of the planet. There is a similar correlation in the 5μm-bright South Equatorial Belt (SEB) between 7°S and 27°S with MWR channels 4, 5 and 6. However, the amplitude of the MWR radiance in the SEB is significantly lower than in the NEB, despite approximately equal 5-μm radiances. There is another faint correlation with bright 5-μm radiances near 35°S. On the other hand, there are faint local maxima in the MWR channels near 28°S, the equator, and (in MWR channel 6) at 22°N that do not correspond to any detectable 5-μm brightening. Figure 2 illustrates that the 5-μm radiances corresponding roughly to the same brightness temperatures, and thus to the same atmospheric depths, as MWR channels 4 and 5. But the correlation between 5-μm brightness and those channels is weak, even accounting for the somewhat larger fields of view. A prominent example of this is the curious depth dependence of the MWR radiances at 5°N - 20°N latitudes. The most straightforward explanation for the loss of correlation between 5-μm and microwave radiation invokes additional opacity arising from particulate absorption and scattering at 5 μm. A similar conclusion arises in the comparison of microwave Very Large Array (VLA) observation by de Pater et al. [2016], which are illustrated together with MWR observations by Janssen et al. [2017b]. Variability of opacity sources in regions that appear to be relatively bright at 5 μm had been noted earlier in high-resolution studies [Bjoraker et al. 2015]. It should be stressed, however, that these authors explicitly describe a "deep" cloud located between 4 and 5 bars (as done also by Giles et al., [2016]), whereas the opacities derived from JIRAM data most likely refer to much higher cloud structures, with effective tops above the 1-bar level. In any case, a straightforward model of an atmosphere with "wet" upwelling winds that loft abundant amounts of condensable gas that form clouds, balanced by "dry" regions with downwelling, desiccated cloudless regions is obviously simplistic. The challenge to modeling will be to examine these results together with appropriate radiative-transfer tools.

Figure 3 illustrates a start in that direction. We compare results for the determination of the abundance of NH_3 gas at the 5-bar level by both JIRAM and the MWR. A set of JIRAM spectra in the range 4.4-5 μm were analyzed by mean of a Bayesian retrieval code specifically developed for the purpose [see also Grassi et al., 2017]. Because of the very different field of views and dwelling times of JIRAM and MWR, it was not possible to acquire simultaneous observations by the two instruments. For a comparison between the two datasets, nominal MWR sampling position and measurement times were considered, and spectra were selected from pixels with the closest spatial correspondence to the MWR track on a fixed-body coordinate system, with longitude adjusted on the basis of average wind field derived from visible observations [Porco et al. 2003] and the time elapsed between JIRAM and MWR observations. Once the longitudes were corrected, pixels within 1000 km from nominal MWR spots were retained for further analysis. Scatter in the retrievals may therefore reflect imperfect motion compensation as well as intrinsic time variability of the atmosphere within the three days of observations.

This spectral region is usually dominated by the thermal emission of the atmosphere and the code has been designed to process only relatively bright spectra, corresponding to moderate (<2) to low opacities, minimizing therefore the residual contribution of scattered solar radiation. In these conditions, the JIRAM data provide information on the deep content of ammonia, the relative humidity of water vapor, the mean content of disequilibrium species (phosphine, germane, arsine) and the residual opacity of clouds, following the approach of Grassi et al. [2010]. For most of the gaseous species, JIRAM data sensitivity peaks between 6 and 3 bars: approximatively, the JIRAM retrievals are representative of mean NH_3 abundance around the 5-bar level. Despite a number of simplifications in the forward modelling of spectra, numerical experiments on simulated observations demonstrated that the *relative* accuracy on retrieved values of ammonia is around 20% and improves to 10% for phosphine and water vapor relative humidity.

Retrievals of the NH_3 VMR from MWR observations follows the approach given in detail by Cheng et al. [2017]. They used a hybrid approach to invert the ammonia distribution. First, the deep ammonia abundance was derived using the nadir brightness temperatures of the six channels near the equator assuming the atmosphere is an ideal moist adiabat because it is the place where the brightness temperatures are lowest. Second, using the deep ammonia abundance derived in the first part, a set of scaling factors were introduced to represent the desiccation of ammonia gas. These scaling factors were then retrieved by matching the brightness temperature spectrum latitude by latitude using the Markov Chain Monte Carlo retrieval algorithm.

Figure 3 compares the results of these approaches. As a whole, the retrieved values are remarkably consistent within their assigned uncertainties, which include estimates of the systematic sources of uncertainty in absolute radiometric calibration for each instrument. The few outliers in the JIRAM retrievals, both above and below the continuous MWR results, could arise from errors in the forward or backward extrapolation of the mean zonal flow that was used to correct the positions of the retrieval locations to points along the MWR track. This might be possible if the flow at the 5-bar level of these retrievals is significantly different from the flow obtained by visible feature tracking by the Cassini imaging team [Porco et al. 2003]. Otherwise values for the NH_3 VMR derived from JIRAM spectra different from the MWR values might arise from ambiguity in differentiating between gaseous NH_3 and otherwise unsuspected absorption or scattering by particulates that is spectrally continuous. In general, however, the consistency of the results provides confidence in this part of the retrieval process that includes the 5-bar region. Overlapping results between 8°N and 9°N, averaging 197±46 ppmv (considering both sampling error and absolute uncertainties) at 5 bars of pressure, are lower than the ~356±70 ppmv derived from the Galileo Probe signal-attenuation experiment by Folkner et al. [1998], with opacity corrections provided by Hanley et al. [2009] (see also Wong et al. [2004] for a summary). However, the MWR results indicate an extremely steep rise with decreasing latitude and a value of 306±30 ppmv closer to the Galileo Probe entry latitude of 6.7°N [Young et al. 1996], yielding overlapping uncertainties with the Galileo results (Figure 3). Verifying the relatively high values for the NH_3 VMR derived by JIRAM poleward of 40°N using MWR measurements awaits further analysis currently in progress.

Finally, we compare the meridional variability of the NH_3 abundance in the deep atmosphere that is derived from the MWR with meridional variations of some gases other than NH_3 that are commonly used as indirect indicators of vertical motions. Figure 4 shows this comparison. Panel A shows the NH_3 VMR retrieved from MWR observations by Li et al. [2017]. We choose the 33-bar level to represent the deep abundance of ammonia gas because it is the

deepest true tie point that was retrieved in the analysis by Li et al. [2017], with values at pressures between the 33 bars and 100 bars, at and below which a meridionally uniform VMR was assumed. Because they did not distinguish between relative errors in the latitude-to-latitude variability, the uncertainties shown represent the absolute uncertainty in the derived values. As noted by Janssen et al. [2017b], Li et al. [2017] and Ingersoll et al. [2017], the morphology of the meridional variability of ammonia abundance at depth is concentrated in a narrow band within 20° latitude of the equator, with the suggestion of a slow increase of the abundance toward higher latitudes starting from a minimum near 20°-25° from the equator. Using the condensate NH_3 as a tracer, this is consistent with substantial upwelling of saturated air from great depth, with the possibility of weaker upwelling increasing from equator to pole. Although a more robust verification of an increase of the NH_3 abundance at this level with latitude must await MWR measurements in later orbits that view higher latitudes with less oblique angles, such an increase is consistent with the generally higher abundances determined by the JIRAM experiment at 5 bars (Figure 3).

Other tracers that have been discussed have included disequilibrium species, such as PH_3, AsH_3, GeH_3, all of which have been detected at the several-bar pressure level or higher, despite being thermochemically unstable at those levels. They are presumed to be present at these levels only because of rapid convection from their thermochemical equilibrium level of ≥1000 K, ≥1 kilobar to upper troposphere [e.g. Barshay and Lewis, 1978] without being destroyed along the way. Phosphine has been detected in the upper troposphere (~500 mbar) using mid-infrared spectroscopy. Panel B shows those results from Fletcher et al. [2016], who derived the PH_3 abundance at 500 mbar from Cassini CIRS observations. The meridional variation is strikingly similar to that of the 33-bar NH_3 abundance shown in panel A: a central maximum is surrounded by a minimum ~15° from the equator and a slow drift toward higher abundances with higher latitudes. These two retrievals and the 5-bar NH_3 abundance shown in Figure 3, comprise a consistent story: a near-equatorial upwelling is implied by both the relatively high abundance of a condensable at 5 and 55 bars and a disequilibrium constituent at 500 mbar, with weaker upwelling increasing toward the poles. However, at greater depths, the retrievals of PH_3 from the 5-μm region by Giles et al. [2016] also show a similar increase toward the poles but without a similar prominent central peak. Not shown here for economy of space are their results for AsH_3, which exhibits a strong equator-to-pole increase without a central peak, and GeH_4, which exhibits an equator-to-pole increase but overlain with what appears as substantial belt-zone variability. Giles et al. caution that their results contain an implicit degeneracy with their solutions for cloud opacity. Although this degeneracy would easily explain the ostensible belt-zone variability, it is not clear whether it could also be responsible for the ostensible differences between PH_3 abundances at 5 bars and 500 mbar. Finally, we consider the para- vs. ortho-H_2 ratio, which is known to vary from its equilibrium value as a function of latitude, also presumed to arise from replenishment from deeper, warmer levels due to upwelling and higher, colder areas due to subsidence that is meridionally variable [Conrath and Gierasch 1984]. Posed in terms of the para-H_2 fraction, we note that values lower than local equilibrium values indicate consistency with equilibrium at higher than ambient temperatures, and vice-versa. Thus, the central drop of the 330-mbar para-H_2 close to the equator in Panel D is consistent with a model of ambient upwelling there. However, its rise toward higher latitudes is consistent with increasing ambient downwelling from colder temperatures. As Conrath and Gierasch [1984] originally pointed out, at this upper part of Jupiter's troposphere, this is likely to be due to overturning of the upwelling material and subsidence from upper-tropospheric and lower-stratospheric levels. This indicates a change of circulation

characteristics between the atmosphere above and below the ~400-mbar radiative-convective boundary.

5 Conclusions

Comparison of high-resolution close-up observation of Jupiter's atmosphere by Juno's remote-sensing instruments verified a significant correlation between regions characterized by visibly dark clouds and high 5-μm thermal brightness, thus associating these low-albedo regions with areas of low cloud opacity of low ammonia gas abundance or both. There are correlations of both visible imaging and 5-μm mapping with regions of low ammonia abundance in the 5-33 bar range derived from microwave mapping. However, there are also significant exceptions that are most likely due to additional particulate opacity sources at 5 μm from small particles to which microwave radiation is insensitive. These results point to the simplistic nature of a model in which upwelling gas always produces high abundances of saturated condensates that form clouds with abundant particulate populations, and downwelling air produces desiccated, cloudless conditions. Measurements of gaseous NH_3 abundance at the 5-bar level from 5-μm JIRAM spectroscopy and MWR radiometry are generally consistent with each other over a wide latitude range. At 5 bars, they are consistent with NH_3 at the lower range of uncertainty of the Galileo probe-relay-attenuation results near the same 6.7°N latitude of the Galileo probe entry. The high abundance of NH_3 near the equator over a broad vertical region is consistent with vigorous upwelling vertical transport and is reflected in the meridional distribution of para-H_2 near 330 mbar and PH_3 at 500 mbar by studies of mid-infrared emission. The absence of such a signature in the meridional distribution of PH_3 near the ~5-bar level could arise from an implicit degeneracy between gaseous and cloud opacity in the analysis of the 5-μm spectroscopy from which it is determined. A slower rise in the NH_3 abundance beginning from a minimum some 20° away from the equator and rising toward the poles is suggested by the comparison of 5-μm and microwave results. It is consistent with a picture of gradually increasing strength of upwelling circulation with higher latitudes, reflected in the general rise of other indirect indicators of upwelling in the troposphere – the increase of abundances of disequilibrium species – PH_3, AsH_3 and GeH_4. However, the opposite is indicated by the slow rise of para-H_2 at the 330-mbar level with latitude, indicating a different dynamical regime in the upper troposphere and lower stratosphere with prevailing downwelling at higher latitudes.

Acknowledgments

A substantial portion of the research was funded by the National Aeronautics and Space Administration through the Juno Project; some of these funds were distributed to the Jet Propulsion Laboratory, California Institute of Technology. The development of JIRAM instrument and the work of Italian co-authors was supported by the Italian Space Agency through ASI-INAF contract I/010/10/0 and 2014-050-R.0. J. G. We are grateful to Leigh Fletcher and to Rohini Giles for numerical version of their results shown in Figure 4. We note that all JunoCam images can be obtained on the Mission Juno web site (https://www.missionjuno.swri.edu), via its links to the JunoCam instrument, then to "Processing".

366

367 **References**

368

369 Acton, C. (1996), Ancillary data services of NASA's Navigation and Ancillary Information
370 Facility, Planetary & Space Sci. 44(1), 65-70, doi: 10.1016/0032-0633995)00107-7
371 Adriani, A., G. Filacchione, T. DiIorio, D. Turrini, R. Noschese, A. Cicchetti, D. Grassi, A.
372 Mura, G. Sindoni, M. Zambelli, G. Piccioni, M. T. Capria, F. Tosi, R. Orosei, B. M.
373 Dinelli, M. L. Moriconi, E. Roncon, J. I. Luninie, H. N. Becker, A. Bini, A. Barbis, L.
374 Calamai, C. Pasqui, S. Nencioni, M. Rossi, M. Lastri, R. Formaro, A. Oliveieri (2014).
375 JIRAM, the Jovian Infrared Auroral Mapper. Space Sci. Rev.
376 doi:10.1007/s11214-014-0094-y.
377 Barshay, S. S., Lewis, J. S. [1978], Chemical structure of the deep atmosphere of Jupiter. Icarus
378 33, 593-611.
379 Bjoraker, G. L., M. H. Wong, I. de Pater, M. Ádámkovics (2015), Jupiter's deep cloud structure
380 revealed using Keck observations of spectrally resolved line shapes, Astrophys. J.,
381 810(2), 122, doi: 10.1088/0004-637X810/2/122.
382 Conrath, B. J. and P. J. Gierasch (1984), Global variation of the para-hydrogen fraction in
383 Jupiter's atmosphere and implications for the dynamics on the outer planets. Icarus 54,
384 187-204, doi10.1016/0019-1035(84)90065-4.

385 de Pater, I., M. Wong, K. de Kleer, P. Marcus. S. Luszcz-Cook, M. Ádámkovics, A. Conrad, X.
386 Asay-Davis, C. Go (2010). Persistent rings in and around Jupiter's anticyclones –
387 Observations and theory. Icarus 210(2), 742-762, doi10.1016/j.icarus.2010-07.027.

388 de Pater, I., M. H. Wong, K. de Kleer, H. B. Hammel, M. Ádámkovics, A. Conrad (2011). Keck
389 adaptive optics images of Jupiter's north polar cap and Northern Red Oval. Icarus,
390 213(2), 559-563, doi10.1016/j.icarus.201.03.006.

391 de Pater, I., R. J. Sault, B. Butler, D. DeBoer, M. H. Wong (2016), Peering through Jupiter's
392 clouds with radio spectral imaging, Science, 352(6290), 1198-1201.

393 Fletcher, L. N., T.K. Greathouse, G. S. Orton, J. A. Sinclair, R. S. Giles, P. G. J. Irwin, T.
394 Encrenaz. (2016a). Mid-infrared mapping of Jupiter's temperatures, aerosol opacity and
395 chemical distributions with IRTF/TEXES, Icarus, 278, 128-161, doi:
396 10.1016/j.icarus.2016.06.008.

397 Fletcher, L. N., I. de Pater, W.T. Reach, M. Wong, G.S. Orton, P.G.J. Irwin, R.D. Gehrz
398 (2016b), Jupiter's Para-H_2 Distribution from SOFIA/FORCAST and Voyager/IRIS 17-37
399 μm Spectroscopy, Icarus, in press doi: 10.1016/j.icarus.2016.10.002.

400 Folkner, W.M., R., Woo, S. Nandi. (1998). Ammonia abundance in Jupiter's atmosphere derived
401 from attenuation of the Galileo probe's radio signal. J. Geophys. Res. 103 (1998), 22847-
402 22856.

403 Giles, R. S., L. N. Fletcher, P. G. J. Irwin (2016), Latitudinal variability in Jupiter's tropospheric
404 disequilibrium species: Ge_4, AsH_3 and PH_3, Icarus, doi: 10.1016/j.icarus.2016.10.023.

405 Grassi, D., A. Adriani, A. Mura, B. M. Dinelli, G. Sindoni, D. Turrini, G. Filacchione, A.
406 Migliorini, M. L. Moriconi, F. Tosi, R. Noschese, A. Cicchetti, F. Altieri, F. Fabiano, G.

Piccioni, S. Stefani, S. Atreya, J. Lunine, G. Orton, A. Ingersoll, S. Bolton, S. Levin, J. Connerney (2017). Preliminary results on the composition of Jupiter's troposphere in Hot Spot regions from the JIRAM/Juno instrument. Geophys. Res. Lett. This issue.

Hanley, T. R., P. G. Steffes, B. M. Karpowicz (2009). A new model of the hydrogen and helium-broadened microwave opacity of ammonia based on extensive laboratory measurements. Icarus 202(1), 316-335, doi:10.1016/j.icarus.2009.02.002

Hansen, C. J., M. A. Caplinger, A. Ingersoll, M. A. Ravine, E. Jensen, S. Bolton, G. Orton. (2014), Junocam: Juno's outreach camera. Space Sci. Rev. ,doi10.007/s/11214-014-0079-x.

Irwin, P. G. J., A. L. Weir, F. W. Taylor, S. B. Calcutt, R. W. Carlson (2001). The origin of belt/zone contrasts in the atmosphere of Jupiter and their correlation with 5-μm opacity. Icarus 149, 397-415 doi: 10.1006/icar.2000.6542.

Janssen, M. A., J.E. Oswald, S.T. Brown, S. Gulkis, S.M. Levin, S.J. Bolton, M.D. Allison, S.K. Atreya, D.Gautier, A.P. Ingersoll, J.I. Lunine, G.S. Orton, T.C. Owen, P.G. Steffes, V. Adumitroaie, A. Bellotti, L.A. Jewell, C. Li, L. Li, S. Misra, F.A. Oyafuso, D. Santos-Costa, E. Sarkissian, R. Williamson, J.K. Arballo, A. Kitiyakara, J.C. Chen, F.W. Maiwald, A.S. Larson, P.J. Pingree, K.A. Lee, A.S. Mazer, R. Redick, R.C. Hughes, G. Bedrosian, D.E. Dawson, W.A. Hatch, D.S. Russel, N.F. Chamberlain, M.S. Zawadski, B. Khayatian, B.R. Franklin, H.A. Conley, J.G. Kempenaar, M.S. Loo, E.T. Sunada, and C.C. Wang (2017a). MWR: Microwave Radiometer for the Juno mission to Jupiter, Space Sci. Rev., In press.

Janssen, M. A., S. J. Bolton, S. M. Levin, V. Adumitroaie, M. D. Allison, J. K. Arballo, S. K. Atreya, A. Bellotti, S. T. Brown, S. Gulkis, A. P. Ingersoll, L. A. Jewell, C. Li, L. Li, J. Lunine, S. Misra, G. S. Orton, T. C. Owen, F. A. Oyafuso, D. Santos-Costa[2] E. Sarkissian, P. G. Steffes, and R. Williamson (2017b), The deep structure of Jupiter's atmosphere as traced by its subcloud ammonia distribution, Geophys. Res. Lett. This issue.

Li, C., A. P. Ingersoll, S. Ewald, F. Oyafuso, M. Janssen (2017). Jupiter's global ammonia distribution from inversion of Juno Microwave Radiometer observations. Geophys. Res. Lett. This issue.

Ortiz, J.L., G. S. Orton, A. J. Friedson, S. T. Stewart, B. M. Fisher, and J. R. Spencer (1998), Evolution and persistence of 5-μm hot spots at the Galileo Probe entry latitude, J. Geophys. Res. 103, 23051-23069, doi: 10.1029/98JE00696.

Orton, G., J. L. Ortiz, K. Baines, G. Bjoraker, U. Carsenty, F. Colas, D. Deming, P. Drossart, E. Frappa, J. Friedson, J. Goguen, W. Golisch, D. Griep, C. Hernandez, W. Hoffmann, D. Jennings, C. Kaminski, J. Kuhn, P. Laques, S. Limaye, H. Lin, J. Lecacheux, T. Martin, G. McCabe, T. Momary, D. Parker, R. Puetter, M. Ressler, G. Reyes, P. Sada, J. Spencer, J. Spitale, S. Stewart, J. Varsik, J. Warell, W. Wild, P. Yanamandra-Fisher, A. Dayal, L. Deutsch, G. Fazio, and J. Hora. (1996), Results of Earth-Based observations of the Galileo Probe entry site, Science 272, 839-840.

Orton, G. S., B. M. Fisher, K. H. Baines, S. T. Stewart, A. J. Friedson, J. L. Ortiz, M. Marinova, W. Hoffmann, J. Hora, M. Ressler, S. Hinkley, V. Krishnan, M. Masanovic, J. Tesic, A.

Tziolas, and K. Parija (1998), Characteristics of the Galileo Probe entry site from earth-based remote sensing observations, J. Geophys. Res., 103, 22791-22814, doi:10.1029/98JE02380.

Owen, T., R. J. Terrile (1981), Colors on Jupiter, J. Geophys. Res. 86, 8797-8814, doi: 10.1029/JA086iA10p08797.

Porco, C., R. A. West, A. McEwen, A. D. Del Genio, A. P. Ingersoll, R. Thomas, S. Squyres, L. Dones, C. D. Murray, T. V. Johnson, J. A. Burns, A. Brahic, G. Neukum, J. Veverka, J. M. Barbara, T. Denk, M. Evans, J. J. Ferrier, P. Geissler, P. Helfenstein, T. Roatsch, H. Throop, M. Tiscareno, A. R. Vasavada. (2003), Cassini imaging of Jupiter's atmosphere, satellites, and rings. Science 299, 1541-1547.

Rayner, J. T., D. W. Toomey, P. M. Onaka, A. J. Denault, W. E. Stahlberger, W. D. Vacca, M. C. Cushing, S. Wang (2003), SpeX: A medium-resolution 0.8-5.5 micron spectrograph and imager for the NASA Infrared Telescope Facility, Pub. Astron. Soc. of the Pacific, 115, 362-382.

Sindoni, G., D. Grassi, A. Adriani, A. Mura, M. L. Moriconi, B. M. Dinelli, G. Filacchione, F. Tosi, G. Piccioni, A. Migliorini, F. Altieri, F. Fabiano, D. Turrini, R. Noschese, A. Cicchetti, S. Stefani, S. J. Bolton, J. E. P. Connerney, S. K. Atreya, F. Bagenal, C. Hansen, A. Ingersoll, M. Jansen, S. M. Levin, J. I. Lunine, G. Orton, A. Olivieri and M. Amoroso, (2017). Characterization of the white ovals on the Jupiter's southern hemisphere using the first data by Juno/JIRAM instrument. Geophys. Res. Lett. This issue.

Terrile, R. J, J. A. Westphal (1977), The vertical cloud structure of Jupiter from 5 micron measurements. Icarus 30,274-281, doi:10.1016/0019-1035(77)90159-2.

Wong, M. H., P. R. Mahaffy, S. K. Atreya, H. B. Niemann, T. C. Owen (2004), Updated Galileo probe mass spectrometer measurements of carbon, oxygen, nitrogen, and sulfur on Jupiter, Icarus, 171 (1) 153-170doi: 10.1016/j.icarus.2004.04.010.

Young, R. E., M. A. Smith, S. K. Sobeck (1996), Galileo Probe: In situ observations of Jupiter's atmosphere, Science, 272, 837-838.

478 **Figures**

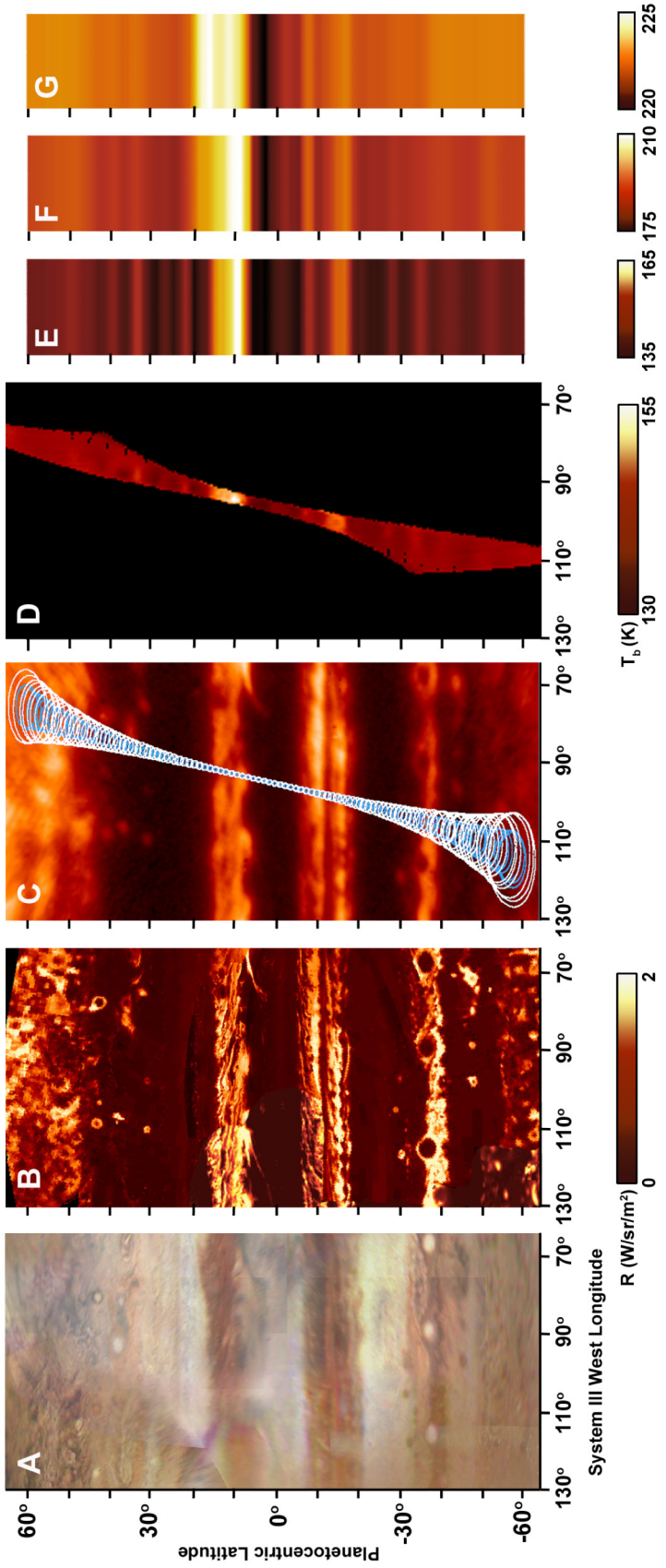

Figure 1. Comparison of different observations of the same region of Jupiter that are contemporaneous with the epoch of perijove 1. Each panel represents a cylindrical projection of imaging or mapping of Jupiter at a different wavelength. Panel A shows a color composite of JunoCam images. Panel B shows a composite of JIRAM 5-μm filter-channel maps, with a high-resolution map mostly covering this region supplemented by an excerpt from a lower-resolution global map filling in. Panel C shows a 5.1-μm cylindrical map projection from an image obtained at NASA's Infrared Telescope Facility approximately 2 hours before perijove (2016 August 27, at 1:18 UT), verifying the forward projection in time of the JIRAM 5-μm observations to the perijove epoch. This panel also illustrates the several positions of the footprints (representing the approximate full-width at half power points) for MWR channel 6 (blue) and channel 1 (white). Panel D shows a map of MWR brightness temperatures in channel 6 (λ=1.37 cm). Panels E, F and G illustrate the meridional variability of zonally-averaged brightness temperature in MWR channels 6, 5 (λ=3.0 cm), and 4 (λ=5.75 cm), respectively. Panels E, F and G are illustrated as extended horizontally as if they were zonal-mean values.

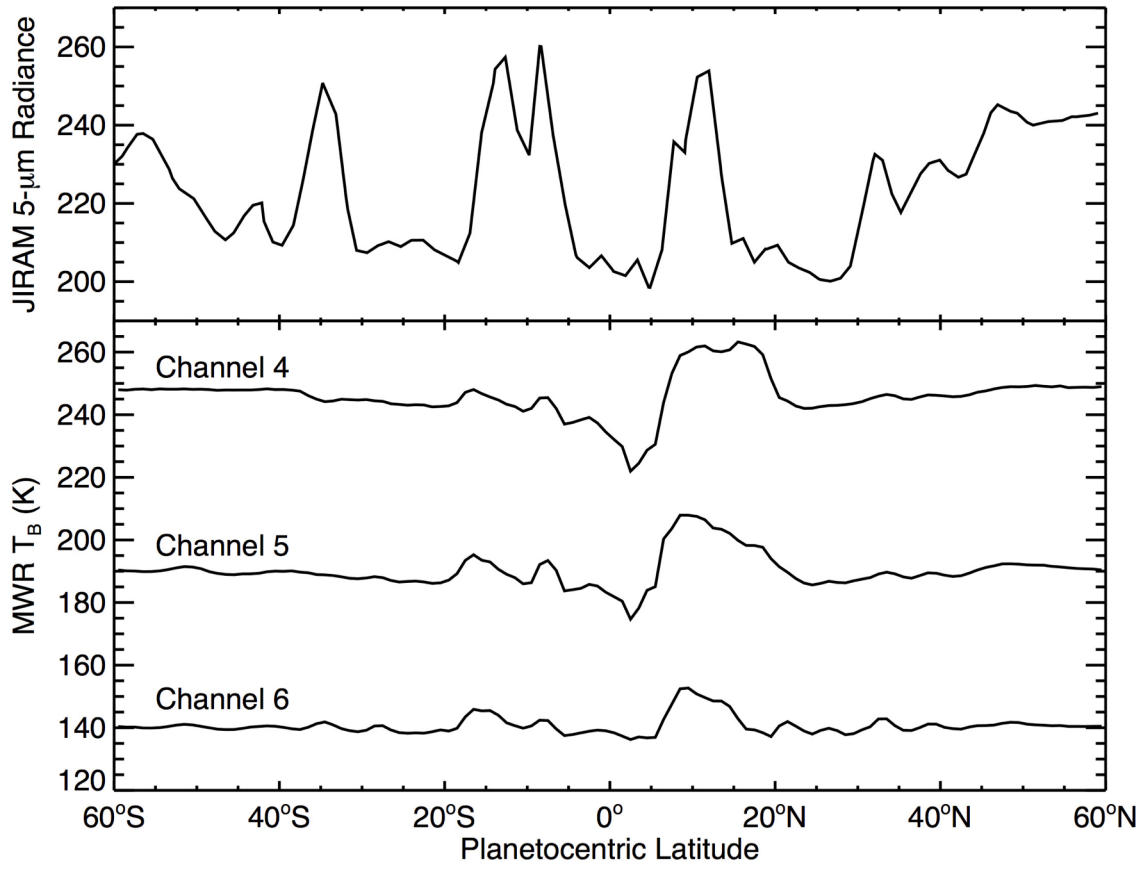

Figure 2. Comparison between the JIRAM equivalent brightness temperatures for5-μm imaging (top panel) and the MWR equivalent brightness temperatures for channels 4 and 5 (bottom panel). The JIRAM brightness temperatures are the result of convolving the high-resolution component of the JIRAM map shown in Figure 1, Panel B, with an MWR angular response function that is an average of those for both channels. The full-width/ half-maximum footprints of these channels are intermediate between those shown for MWR channels 1 and 6 in Panel C of Figure 1. These convolved radiances were then converted to brightness temperatures for consistency with the MWR radiances that are also given in brightness temperatures.

479
480

481

482

483

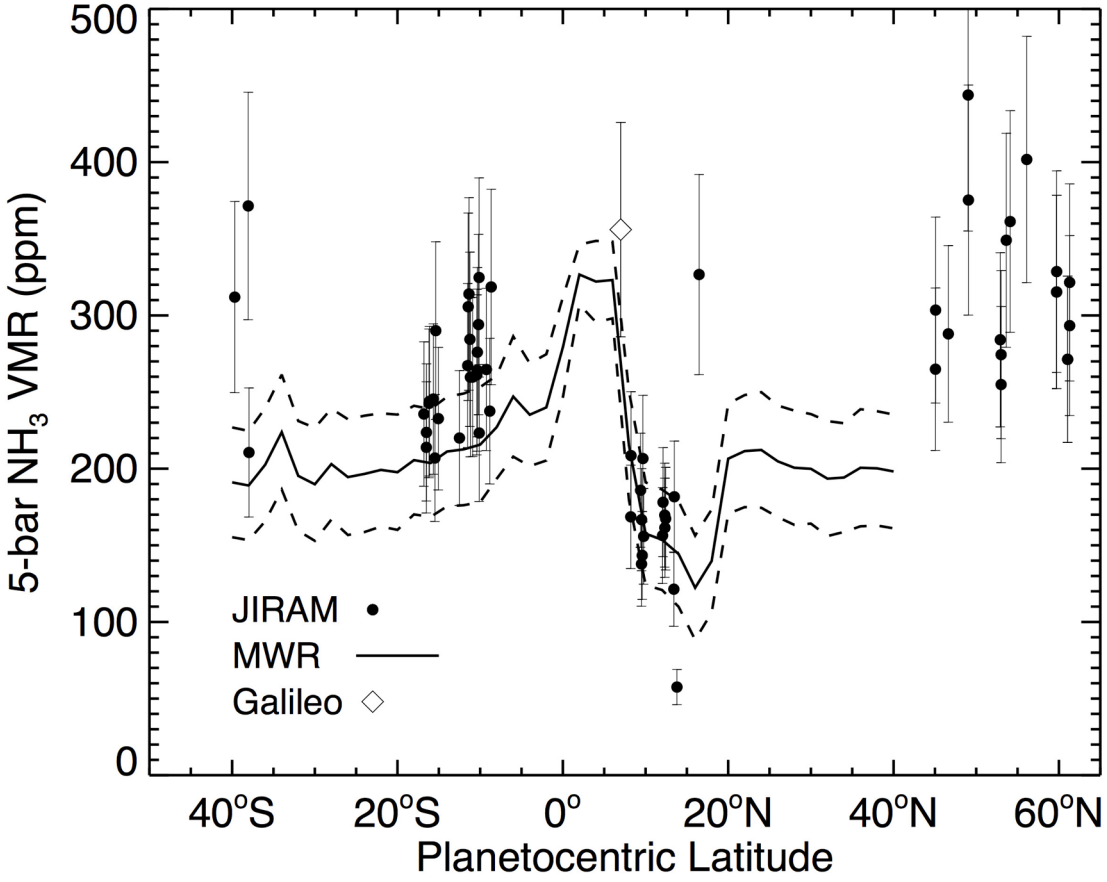

Figure 3. Comparison between retrieved ammonia (NH_3) volume mixing ratio (VMR) from the MicroWave Radiometer (MWR) nadir-equivalent radiometry and JIRAM spectroscopy. MWR results are given by the solid line with the range of uncertainties provided by the dashed lines above and below it. JIRAM results are given for discrete latitudes by the filled circles, with uncertainties denoted by the vertical error bars. Retrievals were not made from latitudes poleward of 40° from the equator in a conservative approach to avoiding any potential interference from synchrotron radiation at this time. Results from the Galileo probe relay attenuation signal experiment at this pressure [Folkner et al. 1998, Hanley et al. 2009] are shown by the open diamond and associated uncertainties.

484

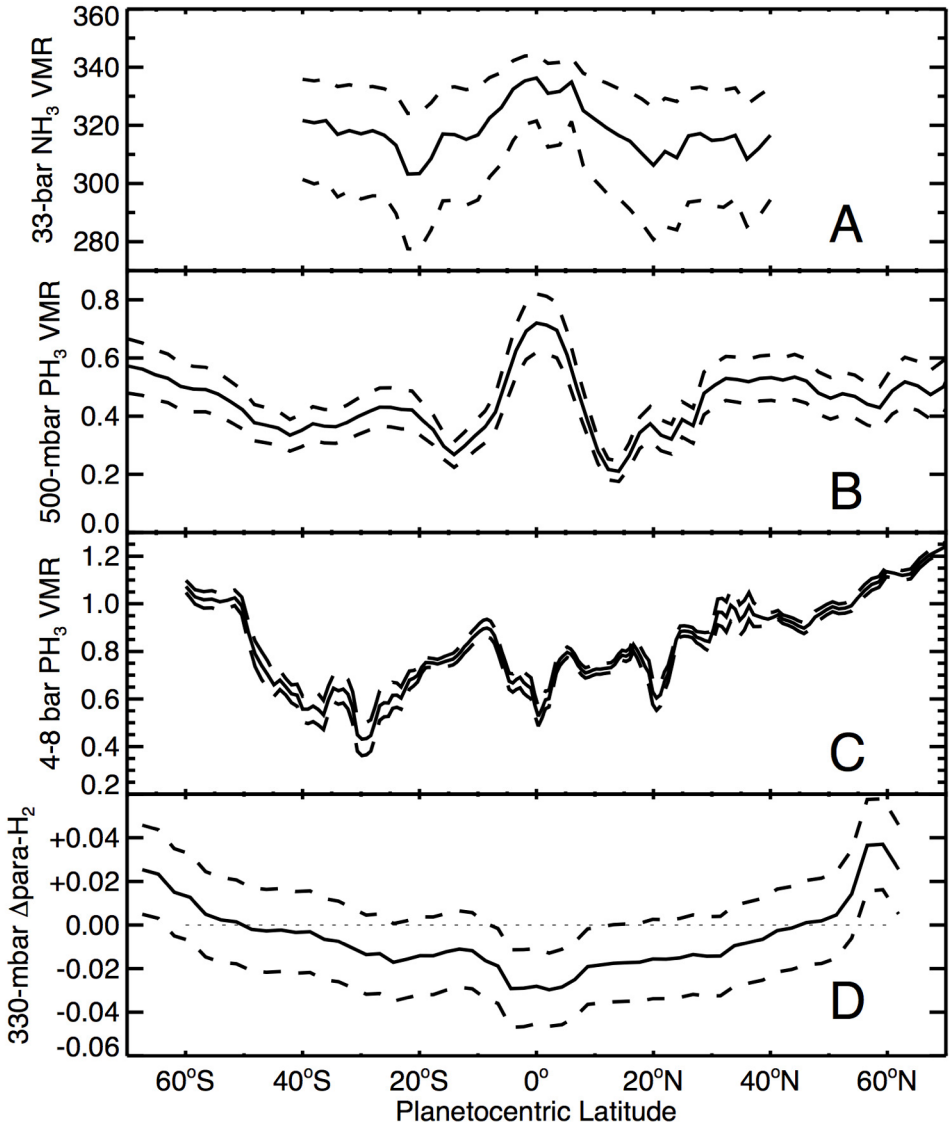

Figure 4. Comparison between the deep NH_3 abundance derived by the MWR experiment and indirect tracers of vertical motions derived from Voyager-1 IRIS observations as a function of latitude. Panel A shows the NH_3 VMR in ppm at an atmospheric pressure of 33 bars derived from the Juno MWR data [Li et al. 2017]. Panel B shows the PH_3 VMR in ppm at 500 mbar atmospheric pressure derived from a re-analysis of Cassini CIRS data by Fletcher et al. [2016a] (see their Fig. 18c). Panel C shows the PH_3 VMR in ppm near 5 bars from the analysis of Very Large Telescope CRIRES observations by Giles et al. [2016] (see their Fig. 16a, black line). Panel D shows the para-H_2 fraction difference from its equilibrium value at 330 mbar atmospheric pressure derived from Voyager-1 IRIS data by Fletcher et al. [2016b]. The range of uncertainties in the derived quantities are shown by the dashed curves. Panel A displays uncertainties in the absolute abundances; the remainder illustrate relative (latitude-to-latitude) uncertainties.